Measuring Irradiance With Bifacial Reference Panels

Riedel-Lyngskar, Nicholas; Bartholomaus, Martin; Vedde, Jan; Poulsen, Peter Behrensdorff; Spataru, Sergiu

Link back to DTU Orbit

Measuring Irradiance with Bifacial Reference Panels

Nicholas Riedel-Lyngskær[1], Martin Bartholomäus[1], Jan Vedde[2], Peter B. Poulsen[1] and Sergiu Spataru[1]

[1]Technical University of Denmark, Department of Photonics Engineering, 4000 Roskilde, Denmark

[2]European Energy A/S, 2680 Søborg, Denmark

Abstract—The heterogenous nature and spectral distribution of rear plane-of-array irradiance R_{POA} presents challenges when measured by small-area sensors such as pyranometers. Bifacial reference modules serving as large-area sensors can simplify irradiance monitoring because their electrical response follows that of the power generating modules in an array. This article compares R_{POA} and effective irradiance G_E measured by calibrated reference modules against three commonly used small-area sensors including pyranometers, reference cells, and photodiodes. A technology-matched monofacial module is mounted side-by-side with the bifacial reference to decouple effective irradiance measurements into front and backside contributions. The results show that R_{POA} and G_E measurements made with reference panels have the best correlation to reference cells. The mean absolute errors between the two measurement approaches are 9% relative, 4 W/m² absolute for R_{POA} and 4% relative, 7 W/m² absolute for G_E. When G_E measurements from the four sensor types are used to predict string-level power, the reference panel measurements show a 3.4% prediction error, which is comparable to that achieved when using G_E measurements from pyranometers (3.0%) and reference cells (2.9%) thereby suggesting that reference modules can be used to accurately measure R_{POA} and G_E in bifacial systems.

Index Terms—Bifacial PV, IEC 60904, rear irradiance, performance ratio, measurement.

I. INTRODUCTION

The commercial rise of bifacial photovoltaic (PV) modules and the growing capacity of bifacial systems [1] has forced the PV community to update several international standards that were initially written for single sided PV devices [2] – [5]. Of interest in this work are the bifacial I-V measurement procedures defined in IEC TS 60904-1-2. Our aim is to assess whether the single-side illumination method described in [2] can be used to calibrate bifacial reference modules that are deployed in large-scale bifacial PV parks to measure effective irradiance.

Accurate bifacial PV modeling can only be achieved when the rear, and ultimately total (i.e., combined front and rear) irradiance is understood, but the PV community is still developing its best-practice guidance on the type, quantity, and placement of sensors for the assessment of rear plane-of-array irradiance (R_{POA}). The many challenges that frustrate accurate R_{POA} measurements are discussed systematically in [6]. Rear-side edge brightening [7], non-uniform irradiance patterns that

change with conditions [8] [9], structural shading effects [10] [11], and in some cases self-shading from a module's frame and/or its conductors make it hardly possible for PV system designers to identify a single small-area location that is representative of the rear array. Ray-trace simulations can be used to determine a suitable small-area sensor location [10], but such methods are prohibitive due to computational intensity, steep learning-curve, and because the results are unique to a given PV substructure design and park layout. Meanwhile, spectral albedo effects [12] – [14] make sensor type selection non-trivial (e.g., pyranometer, reference cell, or Si photodiode).

The literature contains comparisons of small-area irradiance sensors for R_{POA} measurements [15] – [18], works that used monofacial reference modules for frontside plane-of-array irradiance (G_{POA}) measurements [19] [20], and recently, an investigation of bifacial reference panels for effective irradiance monitoring [21].

In this work, we evaluate the potential of bifacial reference panels, calibrated indoors per IEC TS 60904-1-2, to measure rear and effective irradiance. In section III.A, the rear and effective irradiance measurements from reference modules are evaluated against measurements from an array of small-area sensors that includes pyranometers, reference cells and Si-photodiodes. We supplement the analysis in III.A by showing how effective irradiance derived from string-level I-V measurements of a 24-module array compares to the module-level approach. In section III.B, the measurement differences due to spectral albedo effects are estimated using an in-plane spectrometer. The open-circuit voltage (V_{OC}) data from the I-V curves allowed us to calculate the equivalent cell temperature, the results of which are reported on in section III.C. In section III.D, we demonstrate how R_{POA} sensor type and position lead to uncertainty of the bifacial performance ratio (PR_{BIFI}). Finally, section III.E provides comparisons of yield predictions with effective irradiance data from the various sensors against string-level power of an operational system.

II. METHODS

A. Outdoor Measurement Platform

The testbed shown in Fig. 1(a) is located near Roskilde, Denmark (55.6°N, 12.1°E) within the Technical University of Denmark's (DTU) outdoor PV test facility [18] [22]. The 25° fixed-tilt 14.2 kWp grid-tied array contains 24 large-area bifacial PERC (passivated emitter and rear cell) modules that became commercially available in 2021. Each bifacial PERC module contains 120 half-cut G12 (210 mm) wafers. The modules are framed glass/glass, have a 595 W frontside rating at standard test conditions (STC, 1000 W/m², 25 °C, AM1.5G),

and a mean measured P_{MAX} bifaciality coefficient of 0.67 ($\pm$0.02). The market share of such high-power modules based on large-format wafers has grown in the last two years because they have lower production costs per watt and potentially lower balance of system costs [23]. The 2022 ITRPV report states that M10 (182 mm) and G12 (210 mm) wafer sizes will have majority market share from 2022 onward [24].

(a)
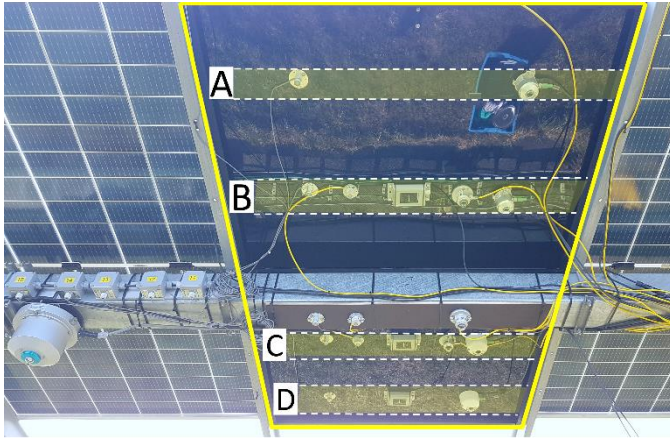
(b)

Fig. 1. (a) The 14.2 kWp bifacial PERC testbed. The monofacial reference panel is highlighted in white, the bifacial reference panel in red, and the rear-side POA sensor plate in yellow. Panels that are not highlighted are connected in series to a grid-tied inverter. (b) Image of the rear POA sensor plate showing spectroradiometer, Si-photodiodes, Si reference cells, and pyranometers. The annotations A through D indicate the sensor locations.

Two reference modules are mounted within the 24-module string and are highlighted with white and red polygons in Fig. 1(a). The reference module highlighted in white was made monofacial by applying several spray-on layers of air-dry Plasti Dip® rubber to the back glass. The reference module highlighted in red was not modified and has the same properties as the other bifacial modules in the string. The monofacial and bifacial reference panels are electrically isolated from the grid-tied string. An EKO PV-Blocks system measures I-V curves of the reference panels every five minutes and holds them at P_{MAX} between I-V scans.

The grid-tied inverter can measure string-level I-V curves. Although most PV inverters have such a hardware capability, this inherent feature is often not used because of software limitations [25]. We perform continuous inverter-level I-V scans

on three select days to estimate the effective irradiance received by the 24-module string, eight of which were calibrated using the IEC TS 60904-1-2 single-side illumination method.

The R_{POA} sensor plate shown in Fig. 1(b) is mounted roughly eight meters from the nearest array edge. We performed ray-trace simulations of the structure in *bifacial_radiance* [26] version 0.3.4 [27] and determined that this location avoids edge brightening. The naming convention we use for the highest to lowest sensor is A to D. The distances between the center beam, where the spectrometer is mounted, and the sensor locations A to D are as follows: A is 77 cm (70%) above, B is 33 cm (30%) above, C is 33 cm ($-$30%) below, and D is 77 cm ($-$70%) below. Table 1 summarizes the sensor types that are used in this work for R_{POA} measurements. The pyranometers and photodiodes are ISO 9060 Class C instruments, while the reference cells meet the Class B requirements defined in IEC 61724-1.

Because IEC 61724-1 states that an optical model can be used to estimate R_{POA} as an alternative to direct R_{POA} measurement, we also present results from a 2D view factor model [28] at array locations A to D. The view factor model takes as input onsite albedo, direct normal (DNI), and diffuse horizontal irradiance (DHI) measurements.

TABLE 1. REAR PLANE-OF-ARRAY SENSORS USED

Instrument	#	Make	Model
Spectrometer	1	EKO	MS-711
Si Photodiode	4	EKO	ML-01
Reference cell	3	IMT	Si-I-420TC-T
Pyranometer	4	EKO	MS-40M

B. Indoor Calibration of Bifacial Reference Panels

The reference panels are of the same make, model, and batch as the 595 W panels within the 24 panel (14.2 kWp) string. Before deployment, a random sample of 10 panels from the batch was selected for flash testing at DTU according to the single-side illumination method described in IEC TS 60904-1-2. The DTU flash solar simulator is a large-area Endeas QuickSun 540XLi (class AAA), which easily accommodates such large (i.e., 1300 mm x 2170 mm) panels. A summary of the flash test results is shown in Table 2. The expanded measurement uncertainty in Table 2 was derived with the methodology proposed by [29]. The uncertainty of backside I-V measurements is higher than frontside because of the increased distance between the reference cell and the cells inside the test module. This effect is caused by the module frame's thickness.

The flasher and measurement method were recently evaluated in a round robin campaign [30] wherein bifacial PV module measurements per IEC TS 60904-1-2 were compared among several accredited European labs. The results showed that DTU's bifacial PERC measurements agreed to the group median within uncertainty for all parameters, which gives us confidence in the reference panel calibration.

Two calibration factors, CF_{Rear} and CF_{Ge}, were derived from the single-side illumination measurements performed indoors. These calibration factors are used to translate the outdoor short-circuit current (I_{SC}) measurements to rear irradiance (R_{POA}) or effective irradiance (G_E), respectively. CF_{Rear} is the linear slope (in A/W·m^{-2}) extracted from the plot of I_{SC} measured at multiple R_{POA} irradiances, with offset forced to the frontside I_{SC}

measured at STC. Similarly, the calibration factor CF_{Ge} is calculated as the linear slope of I_{SC} as a function of single-side equivalent irradiances G_E, with offset forced to zero (see Fig. 4 in IEC TS 60904-1-2 [2]).

TABLE 2. SUMMARY OF I-V MEASUREMENTS MADE ON A SAMPLE OF TEN MODULES (N=10) AT STANDARD TEST CONDITIONS. THE TABLE SHOWS THE MEAN, STANDARD DEVIATION AND EXPANDED MEASUREMENT UNCERTAINTY.

I-V Measurement		Mean	Standard Deviation	Uncertainty (%)
I_{SC} (A)	Front	17.84	0.03	2.2
	Back	11.92	0.09	4.6
V_{OC} (V)	Front	41.05	0.05	0.8
	Back	40.61	0.07	0.9
P_{MAX} (W)	Front	585.91	1.61	3.5
	Back	389.99	3.31	5.5
Fill Factor (%)	Front	80.02	0.19	-
	Back	80.53	0.73	-

C. Irradiance Measurements from Reference Modules and Small-Area Sensors

When analyzing the field measurements, the rear POA irradiance from the reference modules ($R_{POA,Module}$) is determined using (1).

$$R_{POA,Module} = (I_{SC,Bifi} - I_{ISC,Mofi})/CF_{Rear} \qquad (1)$$

Where CF_{Rear} (A/W·m^{-2}) is the calibration factor for rear irradiance, $I_{SC,Bifi}$ (A) is the I_{SC} of the bifacial reference panel, and $I_{SC,Mofi}$ (A) is the I_{SC} of the monofacial reference panel. $I_{SC,Bifi}$ and $I_{SC,Mofi}$ are corrected to 25°C with the datasheet I_{SC} temperature coefficient and back-of-module temperature measurements. The back-of-module temperature sensors are class A PT1000s encased in aluminum housing and attached to the center of the module's back glass with adhesive.

The bifacial reference panel measurements provide a direct estimate of effective irradiance with (2).

$$G_{E,Module} = I_{SC,Bifi}/CF_{Ge} \qquad (2)$$

Where $G_{E,Module}$ (W/m^2) is the effective irradiance measured by a single reference module, or string of modules, CF_{Ge} (A/W·m^{-2}) is the calibration factor for total effective irradiance, and $I_{SC,Bifi}$ is the I_{SC} of the bifacial reference panel, or string. G_E comparisons between the large-area modules and small-area sensors are possible with (3).

$$G_{E,Sensor} = G_{POA} + \varphi \cdot R_{POA} \qquad (3)$$

In (3) G_{POA} (W/m^2) is the frontside POA irradiance, φ is the I_{SC} bifaciality coefficient at STC (0.67 ±0.02), and R_{POA} (W/m^2) is the average rear-side POA irradiance at locations A to D measured by a given small-area sensor type. G_E calculated with (3) uses a consistent sensor type for G_{POA} and R_{POA}. For example, when using (3) to calculate G_E with reference cells, the G_{POA} data comes from a reference cell mounted on the frontside POA that is of the same make and model of those used to measure R_{POA}. In the case of G_E with pyranometers, we use measurements from a class A pyranometer for G_{POA} in (3).

III. RESULTS

The data presented here were recorded from January 4th to May 17th, 2022. Neither the sensors nor the modules were cleaned regularly, but frequent rainfall in Denmark's humid continental climate leads to minimal soiling ratios throughout the year. This assumption was verified with soiling ratio (SR) measurements from a DustIQ optical sensor [31]. The mean SR during the test period was 0.997, with a minimum of 0.992.

We apply two data filters in the analysis. First, data are removed when the angle of incidence (AOI) between the array and the Sun's beam component is greater than 80°. Secondly, an irradiance stability filter removes data when global horizontal irradiance (GHI) measurements sampled at 1 Hz vary by more than 15 W/m^2 within a ±15 second period around each R_{POA} measurement.

A. Rear and Effective Irradiance (R_{POA} and G_E)

Fig. 2 shows exemplary R_{POA} and G_E measurements on three mostly sunny days. The diurnal profiles in Fig. 2 were selected to demonstrate results under different solar zenith
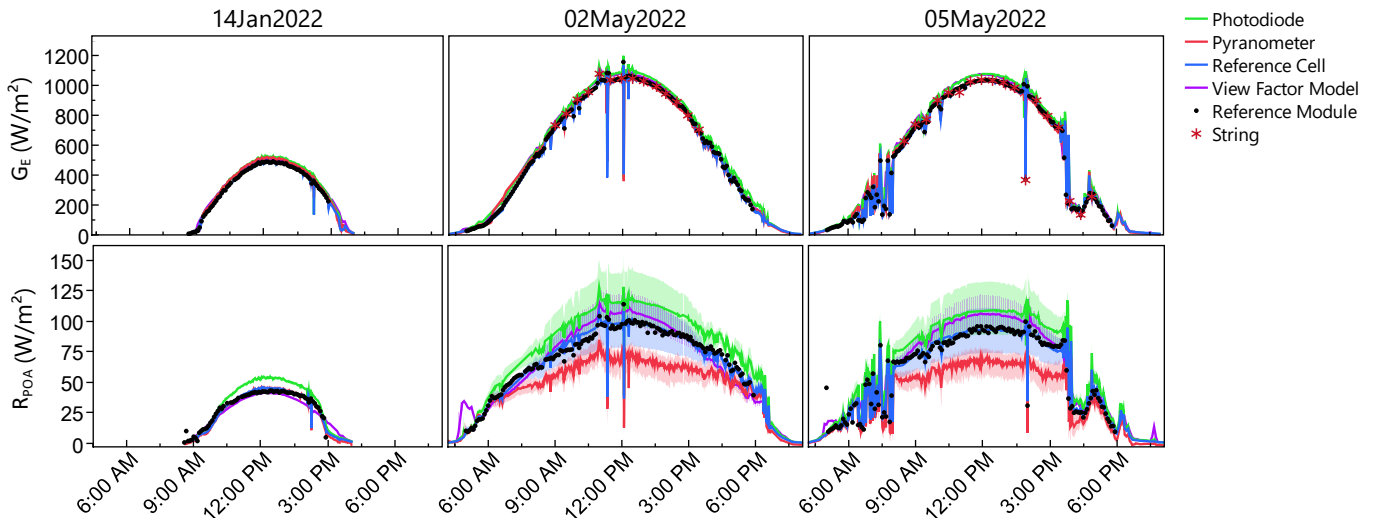

Fig. 2. Timeseries of effective irradiance (G_E) and rear irradiance (R_{POA}) on three mostly sunny days. The semi-transparent bands around R_{POA} timeseries represent the range of values measured at the sensor positions shown in Fig. 1(b). The reference cells, pyranometers, and photodiodes are sampled every minute. The reference modules are sampled every five minutes. The string I-V is performed every 30 minutes on the selected days.

angles, and to show two days when string-level measurements were performed for G_E estimation (May 2nd and May 5th). The solar elevation peaked at 13° on January 14th and at 51° on May 5th, which explains why light intensity in May is about double what it is in January. The semi-transparent bands around the R_{POA} timeseries represent the range of values measured at the 3–4 locations shown in Fig. 1(b).

The photodiode measurements show a positive bias relative to other R_{POA} and G_E methods. In Section III.B, we quantify that up to 10% of the bias in R_{POA} measurement is due to spectral albedo effects. There are other reasons for the differences in R_{POA} measurement that we have not quantified including the different calibration sources and the nonlinearity of signal-to-irradiance relationships. The different directional responsivities of the sensors are not likely causing significant R_{POA} measurement discrepancies because the sensors on the rear-side receive only diffuse light for practically the whole test period. The reference cells have embedded temperature sensors, which are used to translate their output to 25°. The readings from these embedded sensors were between −6 °C and 26 °C. Such a temperature range could change the pyranometer readings up to 3% while causing minimal change to the photodiode outputs, according to the instruments' datasheets.

Fig. 3 shows the differences between R_{POA} measured with the various small-area sensors and R_{POA} measured with the large-area reference modules. Modeled R_{POA} at locations A to D using the view factor approach are shown for reference. The differences between methods are shown as cumulative distribution functions (CDFs). CDF curves with steeper slopes indicate distributions with lower variances. The reference cell group shows the steepest slope of all groups with 80% of the measurements agreeing to the reference module measurements within ±5 W/m². The reference cell group also shows the lowest median bias (0.7 W/m²) of all small-area methods tested. The pyranometer, view factor and photodiode methods show median biases of −2.4 W/m², 5.5 W/m², and 7.5 W/m² relative to the reference module, respectively. The good agreement of the reference cell and reference module approaches is not surprising given that the two device types share similar—but not identical—spectral, directional, thermal, and temporal responsivities.

The R_{POA} sensor plate in Fig. 1(b) lacks a reference cell at location A. Our ray-trace simulations showed that light intensity on the top half of the system (i.e., locations A and B) is more homogenous than the bottom half (i.e., locations C and D). Therefore, a reference cell placed at location A would likely have yielded R_{POA} results comparable to that of location B.

Fig. 4 shows how the reference module G_E measurements compare to three small-area G_E measurement approaches and to G_E simulated with the view factor model. Only four curves are displayed in Fig. 4 since R_{POA} in Equation (3) is the average of the 3–4 small-area locations. The reference cell measurements again show the best agreement to the module-based measurements, with 83% of the measurements within ±10 W/m². Although the pyranometer and reference cell measurements show median biases near zero (i.e., −1.1 W/m² and −0.4 W/m²), the pyranometers show about twice the dispersion, with 77% of measurements within ±20 W/m² of the reference module G_E measurements.
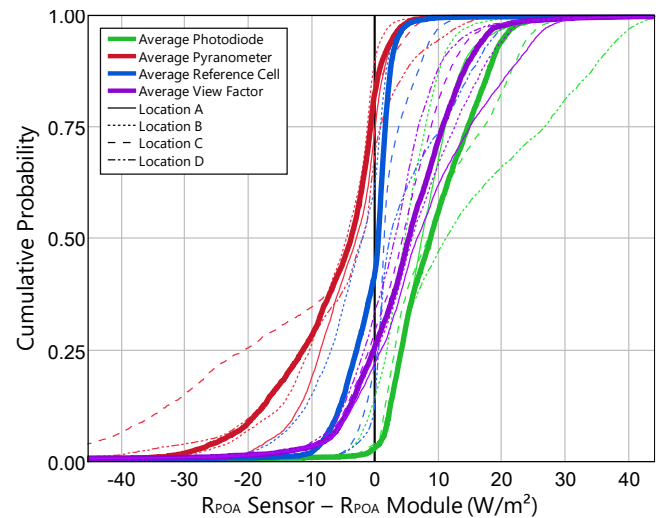

Fig. 3. Cumulative distribution functions of the R_{POA} differences between four small-area measurement\simulation methods and the reference modules. The thick solid lines show the average of 3–4 locations within a given method.
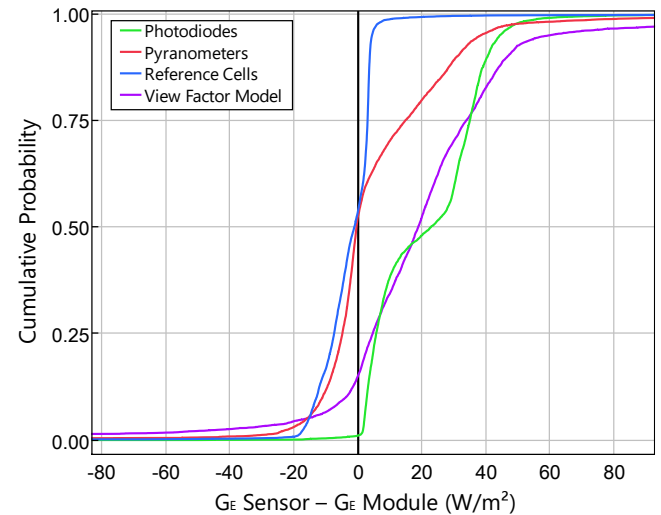

Fig. 4. Cumulative distribution functions of G_E differences between small-area measurement\simulation methods and the reference module.

Fig. 5 summarizes the differences between the small-area methods and the reference module measurements in terms of mean bias error (MBE), mean absolute error (MAE), and mean absolute percentage error (MAPE). The MBE values are comparable to the 50% values of the CDFs in Fig. 3 and Fig. 4, but there are small deviations because the distributions are non-normal.

Fig. 5 shows that the reference cell approach nearly always gives the lowest MBE, MAE and MAPE of all methods, regardless of the reference cell's rear-side location. The lowest MAE and MAPE are achieved when the reference cell is placed at location B (+30% from center) or location C (−30% from center). This suggests that a reference cell placed at one, or both, locations could serve as a representative location of the effective rear-side irradiance – so long as the fixed-tilt substructures are geometrically similar to those used here. This result differs from [10] where ray-trace simulations suggested that, for single-axis trackers, placing irradiance sensors at 20% from the array edges yields the closest value to the average.

However, the result in this work is consistent with [32] where ray-trace simulations suggested that, for four-in-landscape fixed tilt systems, placing rear-side sensors 68% from the lower edge is representative of the average irradiance. Location B in Fig. 1(b) is 65% from the lower edge.

A comparison of bifacial modules and pyranometers for G_E measurements on trackers was recently performed by [21]. Their results showed pyranometer G_E was on average 3.6% higher than reference module G_E. The results in Fig. 5 show a 6.6% MAPE for pyranometer versus reference module G_E. Adjustments for AOI and spectral dependencies were made to the pyranometer G_E in [21], but were not done here, which may be the cause of discrepancy between the two works.
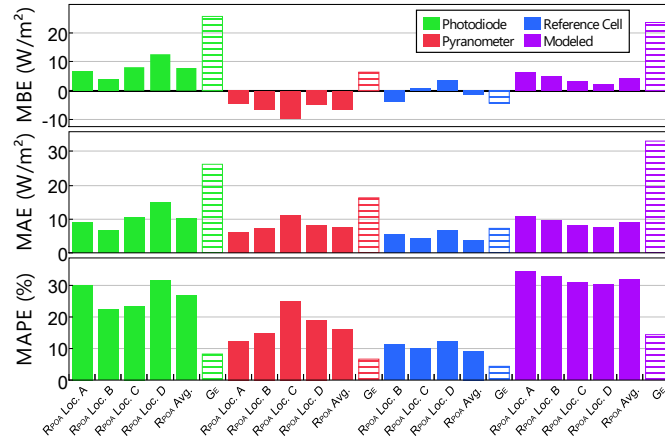

Fig. 5. Error summaries for R_{POA} and G_E measurements using various methods. The mean bias error (MBE), mean absolute error (MAE), and mean absolute percentage error (MAPE) for each method and location are relative to the reference module results. The solid bars show R_{POA} and hatched bars show G_E.

Having established that the reference cell and reference module measurements show the strongest correlation for R_{POA} and G_E, we now provide a deeper look at their relationships. Fig. 6 shows the difference between R_{POA} measured by the reference module pair and R_{POA} measured by the reference cells (average of locations B and C). The color scale in Fig. 6 reveals that the R_{POA} residuals have a dependence on the ratio of DHI to GHI, also known as the diffuse fraction (F_D).

Fig. 7 shows the difference between G_E measured by the bifacial reference module and G_E from the monofacial reference cell measurements calculated with (3). The difference between reference module and reference cell G_E measurements is less than 1% when AOI is less than 30° and the irradiance is between 900 and 1100 W/m². The reference panels have an antireflective coating (ARC) on the front glass whereas the reference cells do not. This means that the I_{SC} of the two devices may not follow the same AOI dependency.

The green asterisks in Fig.7 show G_E results using string-level I_{SC} measurements on three days. The trend of the string-level measurements mostly follows that of the module-level measurements. However, larger differences sometimes occur, which may be attributed to differences in I_{SC} between modules within the string, edge brightening effects, and\or time synchronization between measurements.
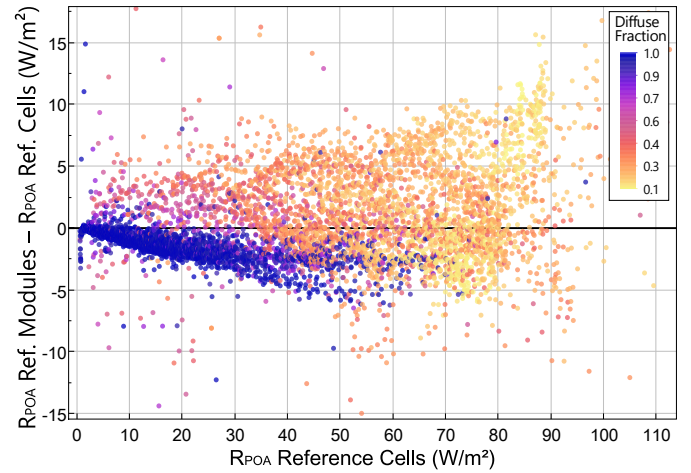

Fig. 6. Difference between R_{POA} as measured by the large-area reference module pair and R_{POA} measured with small-area reference cells. The x-axis shows the average of reference cell R_{POA} measurements at locations B and C. The color scale shows the fraction of diffuse light in the sky hemisphere.
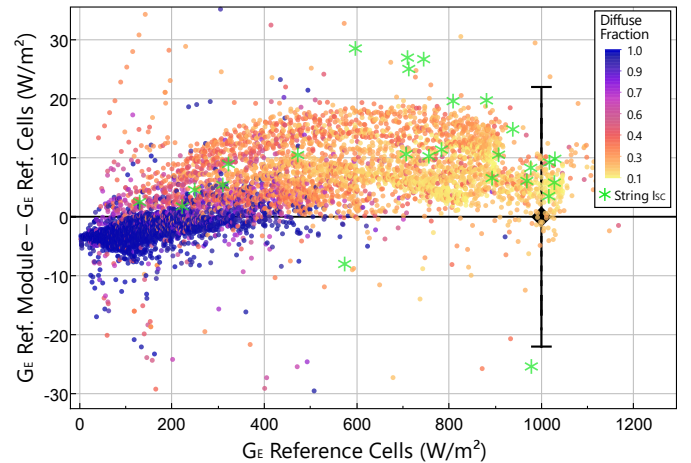

Fig. 7. Difference between G_E as measured by the large-area bifacial reference module and G_E measured with small-area reference cells. The asterisk symbols indicate G_E calculated from string-level I_{SC} measurements on select days. The x-axis shows G_E from the reference cell measurements. The error bars at 1000 W/m² represent the ±2.2% uncertainty of the laboratory measurement of I_{SC} at STC. The color scale shows the fraction of diffuse light in the sky hemisphere.

B. Spectral Implications

Here we show how spectral effects can influence the sensor outputs. Fig. 8(a) shows typical R_{POA} spectra recorded during green vegetation—the predominant albedo during the measurement campaign—and a condition with partial snow coverage. Consistent with [12] – [14], the green grass R_{POA} spectrum displays a heavy redshift relative to the AM1.5G reference spectrum. Snow spectra such as that shown in Fig. 8(a) were observed on three days during the test period. Such spectra demonstrate how significantly the redshift is reduced during snow conditions. Fig. 8(b) shows the spectral responsivities (SR) of the various devices used in this work. The PERC cell's backside SR is taken from the PERC measurements performed in [14], the photodiode and pyranometer SR files were provided by the manufacturer, and the reference cell SR was digitized from the datasheet.
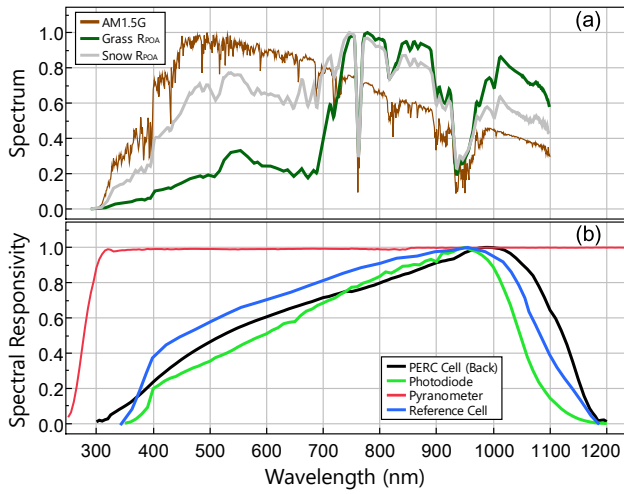
Fig. 8. (a) normalized rear-side spectral irradiance measured at midday on clear days with green grass albedo and when the ground is partially covered in snow. The AM1.5G calibration spectrum is shown to illustrate the spectral shifts observed in the field. (b) normalized spectral responsivity of a PERC cell's backside, photodiodes, pyranometers and reference cells used in this work.

With the continuous in-plane spectral measurements and equation 7 of IEC 60904-7 [33], we derive spectral mismatch (SMM) for the rear-side POA.

$$Rear\ SMM = \frac{G_{Ref} \cdot \int_a^b SR(\lambda) \cdot R_{POA}(\lambda)d\lambda}{R_{POA} \cdot \int_a^b SR(\lambda) \cdot G_{Ref}(\lambda)d\lambda} \quad (4)$$

$SR(\lambda)$ is the normalized device spectral responsivity, $R_{POA}(\lambda)$ is the normalized rear-side spectral measurement recorded every five minutes, and $G_{Ref}(\lambda)$ is the normalized AM1.5G reference spectrum [34]. The 300 nm to 1100 nm integration limits are determined by the sensitive range of the spectroradiometer. In (4), R_{POA} is calculated as the integral of $R_{POA}(\lambda)$ and G_{Ref} is calculated as the integral of $G_{Ref}(\lambda)$ over the same integration limits. SMM values greater than 1 indicate spectrally induced gains in photocurrent relative to AM1.5G, and SMM values less than 1 indicate spectrally induced losses. If SMM is ignored, the fractional measurement error due to spectral shift is 1 – SMM.

Fig. 9 shows the relationships between the rear-side SMM factors of each device type shown in Fig. 8(b). Each data point in Fig. 9 is calculated with a single rear-side spectral measurement. Fig. 9 therefore contains 2,655 rear-side SMM factors, for each device, that collectively represent the actual spectral conditions recorded during the four-month test period. The contours around regression lines in Fig. 9 highlight 90% of the SMM values. When snow conditions were present, the rear-side SMM of the Silicon-based sensors is less than 1.10.

The photodiode shows the highest SMM due to its narrow SR and weak response in the visible spectrum (400–700 nm). Some commercially available photodiode models have a lower visible light SR than that shown in Fig. 8(b) [35]. For such devices, we calculated SMM as high as 1.5 with our R_{POA} spectra above green grass. The reference cell SMM is 8% to 11% lower than that of the photodiode. When the reference cell and photodiode measurements are adjusted by a factor of 1/SMM, then the R_{POA} differences shown in Fig. 2 are reduced in half. The remaining differences may be due to different calibration sources.
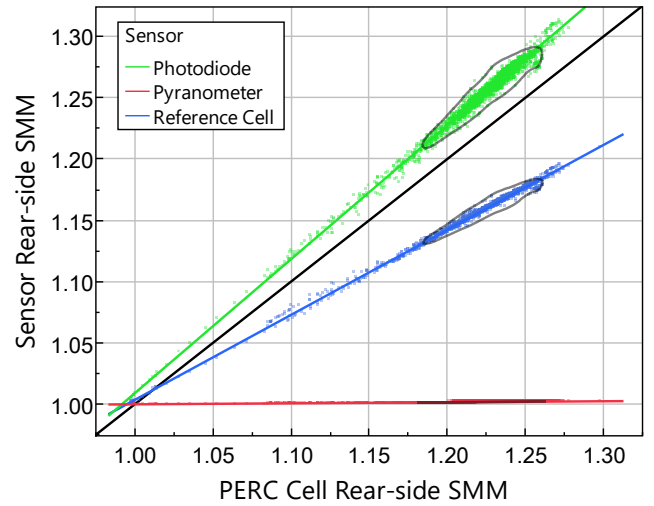

Fig. 9. Bivariate of spectral mismatch (SMM) calculated with the rear-side spectral measurements during the 4-month test period. The regression shows rear-side SMM of the photodiode, pyranometer, and reference cell versus the rear-side SMM of a PERC cell. The black 45° line indicates a spectral match to the PERC cell's rear side. The contour around each regression line indicates where 90% of the SMM values are located.

Fig. 9 shows that the reference cell SMM is 5% to 7% lower than PERC cell backside. In other words, the two are not spectrally matched and 5% to 7% of the measured differences are attributable to spectral effects. Although this result runs counter to the common perception that silicon reference devices are similar enough to silicon power-generating devices such that no spectral corrections are needed [36], R_{POA} is typically an order of magnitude less than G_{POA}. Therefore, spectral errors in R_{POA} measurements are likely to impact yield predictions of bifacial PV systems by less than 1%.

Equation (4) assumes that the reference device is spectrally flat. Apart from some absorption of UV light, the pyranometer used in this work has a spectrally flat response and therefore its rear-side SMM is always near 1, wherein 90% of values are between 1.001 and 1.002. The spectroradiometer's 300 – 1100 nm sensitive range presents limitations because the pyranometer has a 280 – 3000 nm spectral range. However, rear-side SMM calculated over the full 280 – 3000 nm range was comparable (1.002) when using AM1.5G multiplied by the green grass spectral albedo from SMARTS as $R_{POA}(\lambda)$ [37].

C. Equivalent Cell Temperature (ECT) Results

Back-of-module temperature (T_{MOD}) measurements performed on bifacial modules will inevitably partially-shade some active area. The shading induced by a single T_{MOD} sensor is not likely to create local hotspots when albedo is low (i.e., < 0.3). However, bifacial T_{MOD} measurements during high albedo conditions such as snow, or during periods when the sun is behind the PV structure, may put the partially shaded cell into reverse bias. The V_{OC} data from the reference panels and string offer an opportunity to avoid rear-side sensor shading by calculating T_{MOD} with the equivalent cell temperature (ECT) approach [38]. Here we describe our experience applying the ECT procedures to the outdoor V_{OC} measurements of a single bifacial module, and to a string of 24 bifacial modules with (5).

$$ECT = T_{STC} + \frac{1}{\beta}\left[\frac{V_{OC}}{V_{OC,STC}} - 1 - a \cdot \ln\left(\frac{G}{G_{STC}}\right)\right] \qquad (5)$$

According to [38], ECT in (5) represents the average temperature (°C) at the p-n junctions within a module or array, V_{OC} is the outdoor measured open-circuit voltage (V), β is the temperature coefficient of V_{OC} (1/°C), T_{STC} is 25 °C, $V_{OC,STC}$ is the open-circuit voltage measured at STC in the lab (V), G_{STC} is 1000 W/m^2, G is the irradiance (W/m^2), and a is a dimensionless parameter that depends on the module's voltage-irradiance response. The value for the a coefficient was determined from our laboratory measurements at 200 W/m^2 and 800 W/m^2. We applied a self-referencing approach by substituting G with the field measured I_{SC}, and G_{STC} with the lab measured $I_{SC,STC}$. We looked to recent literature [39] to find a representative β value for PERC (−0.31%/°C) as the DTU lab is not equipped to measure β of the large-area 595 Wp modules.

For single panel ECT measurements, the error (ECT − T_{MOD}) is calculated with a single PT1000 sensor on the bifacial reference panel, while for string-level ECT measurements, the error is with the average of four PT1000 measurements across the string (Fig. 1a). We adjust the back-of-module surface temperature T_{MOD} to cell temperature using the King model [40] for glass-glass modules, which adds an offset of 3 °C · (G_E/1000 W/m^2) to the measured T_{MOD}. A recent field trial [41] showed that this simplistic approximation of cell temperature is reasonably accurate.

Fig. 10 shows the difference between ECT and T_{MOD} when $G_E \geq 200$ W/m^2. In this irradiance range, the MAE is 2.5°C and 2.1°C for the module and string measurements, respectively. The MBE is similar at 2.4°C and 2.1°C, respectively. The error has a positive correlation with irradiance.

There are several uncertainty contributions that must be considered when evaluating the error, including the ECT model parameter values, the temperature non-uniformity of cells within a module, the difference between back-of-module surface and p-n junction temperature, the PT1000 sensor accuracy, and the thermal contact between PT1000 sensor and module surface.
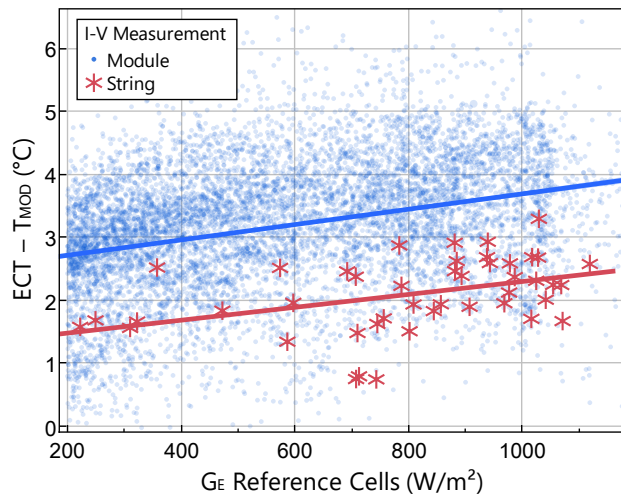
We found that the ECT model is most sensitive to the value of the $V_{OC,STC}$ and β. For example, the expanded uncertainty of the $V_{OC,STC}$ measurements is ±0.8% (i.e., ±0.3 V for a single module). Varying $V_{OC,STC}$ within uncertainty results in a ±2.4° change in ECT. Meanwhile, the stated accuracy of the class A PT1000 sensors used to compare to the ECT method is ±1°C. Given, the many uncertainties, our results suggest that the ECT method via V_{OC} measurements is a practical approach for monitoring bifacial module temperature. Previous works have proposed that the ECT method is more accurate than direct T_{MOD} measurements of monofacial modules [42], largely because of the challenges and uncertainties associated with direct T_{MOD} measurements [43].

D. Bifacial Performance Ratio (PR_{BIFI})

IEC 61724-1 [3] states that the classic performance ratio (PR) formula [44] can be transformed to bifacial PR (PR$_{BIFI}$) if an adjustment is made for the rear irradiance. This is done in practice by multiplying G$_{POA}$ by a factor of either *BIF$_{sensor}$* or *BIF$_{module}$*. When small-area sensors such as reference cells are used to measure R$_{POA}$, (6) is used to calculate BIF$_{sensor}$.

$$BIF_{sensor} = (1 + \varphi_{pmax} \cdot \rho_i) \qquad (6)$$

Where bifaciality φ_{pmax} is the ratio of rear to frontside P$_{MAX}$ at STC and the optical gain ρ_i is the ratio of R$_{POA}$ to G$_{POA}$. When the reference modules are used to derive PR$_{BIFI}$, BIF$_{module}$ is calculated with (7).

$$BIF_{module} = \frac{I_{SC,Bifi}}{I_{SC,Mofi}} \qquad (7)$$

Where $I_{SC,Bifi}$ and $I_{SC,Mofi}$ are the I_{SC} measurements of the bifacial and monofacial panels, respectively. Since R$_{POA}$ from small-area sensors is used to calculate PR$_{BIFI}$ with (6), the question arises: which R$_{POA}$ location to use and from which sensor type?
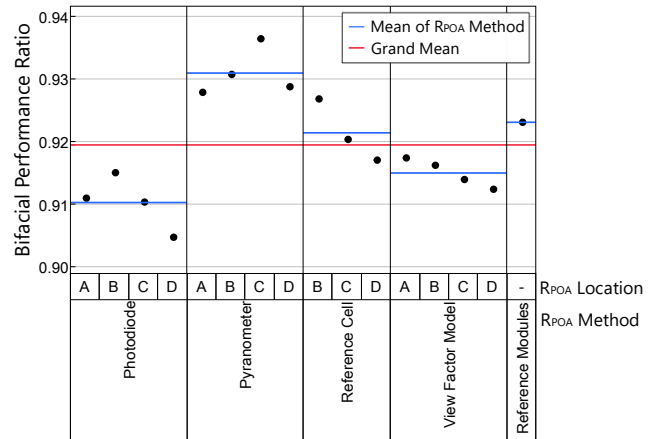
Fig. 11. Variability of the bifacial performance ratio PR$_{BIFI}$ calculated according to the IEC 61724-1 using three small-area sensor types, an optical model, and a reference module pair. All sensors are eight meters from the nearest array edge. See Fig. 1(b) for illustration of R$_{POA}$ sensor locations A to D.

Fig. 11 shows the 14.2 kWp system's PR$_{BIFI}$ calculated with the five methods and four rear-side locations used in this work. Frontside G$_{POA}$ from the same Class A pyranometer is used in all calculations, which means that all variation of PR$_{BIFI}$ in Fig. 11

Fig. 10. Errors between the equivalent cell temperature (ECT) method and back of module temperature (T_{MOD}) measurements applied to a bifacial module and a bifacial string. The x-axis shows effective irradiance (G_E) calculated with reference cell measurements. The data shown here includes four months of module measurements and three days of string-level measurements.

is caused by the R_{POA} measurement used. Fig. 11 shows that PR_{BIFI} differs up to 3% with the R_{POA} methods considered here. The 14.2 kWp system used for study has a 1.7 m ground clearance, which is higher than typical utility-scale fixed tilt systems. The spread of possible PR_{BIFI} values is likely to increase with lower ground clearance because nonuniformity of R_{POA} will be higher [8] [32].

E. Comparisons of Measured and Modeled DC Power

Here we compare the measured DC power of the 14.2 kWp string to modeled DC power using the various G_E measurement methods. We model DC power using the PVWatts model [45], which calculates DC power with (8).

$$P_{DC} = \frac{G_E}{1000\ W/m^2} \cdot P_{STC}[1 + \gamma \cdot (T_{Mod} - 25\ °C)] \quad (8)$$

Where P_{DC} (W) is the modeled string-level DC power, G_E (W/m^2) is the effective irradiance from either the bifacial reference module, reference cells, pyranometers, or photodiodes, P_{STC} (W) is the average module power measured at STC (Table 2) multiplied by the number of modules in the string, γ (%/°C) is the temperature coefficient for power, and T_{MOD} (°C) is the module temperature measured at four locations on the back of the array.

Equation (8) does not account for angular-dependent reflection losses, spectral shifts, or low-irradiance performance. Therefore, the results shown in Fig. 12 only contain data where AOI < 45°, optical air mass (AM) is between 1 and 2, and G_{POA} > 700 W/m^2. Recall that G_E calculations for pyranometers use frontside G_{POA} from a class A device and use the average of class C devices for R_{POA}.

Table 3 shows the error summary when the various G_E data sources are used to predict string-level power. The mean absolute error (MAE) and mean bias error (MBE) are normalized to the 14.2 kWp rating of the modeled array. The results show that photodiodes yield the highest MAE, MBE and MAPE, which is consistent with the comparisons shown in Fig. 2 through Fig. 5. The normalized MAE and MAPE are all within about 0.5% when the pyranometers, reference cells and reference modules are used for G_E in the modeling. However, the reference cell data provides the lowest bias relative to the field measurements.
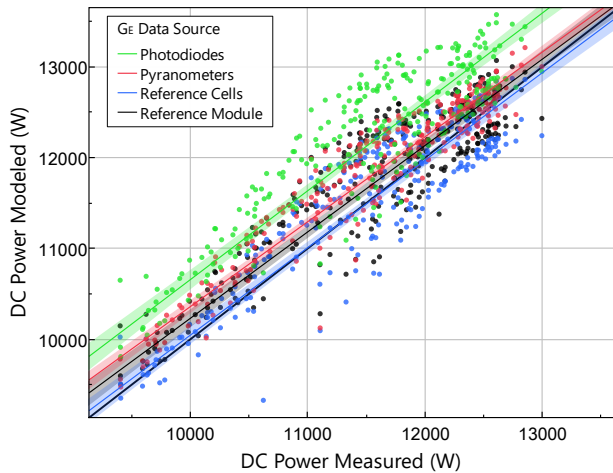

Fig. 12. Bivariate regressions of modeled DC power using four different sources for effective irradiance versus measured DC power.

TABLE 3. ERROR SUMMARY RESULTING FROM USE OF DIFFERENT G_E DATA SOURCES WHEN MODELING DC POWER. THE MEAN BIAS ERROR AND MEAN ABSOLUTE ERROR ARE NORMALIZED TO THE 14.2kW RATING OF THE ARRAY.

G_E Data Source	MBE (W/kWp)	MAE (W/kWp)	MAPE (%)
Photodiodes	46.4	49.1	6.1
Pyranometers	19.0	23.6	3.0
Reference cells	1.2	23.3	2.9
Reference module	13.2	27.0	3.4

IV. DISCUSSION

We have compared rear plane-of-array (R_{POA}) and effective irradiance (G_E) measurements made with calibrated reference modules against measurements from small-area sensors that included photodiodes, pyranometers and reference cells. The results showed that the reference cell R_{POA} and G_E measurements had the strongest correlation to R_{POA} and G_E measured with reference modules. The average agreement between the two approaches was 9% relative, 4 W/m^2 absolute for R_{POA} and 4% relative, 7 W/m^2 absolute for G_E. We found that reference cells located at ±30% from the center of the fixed-tilt array had the best agreement to the reference module R_{POA} measurements. Thus, a single small-area rear facing reference cell can provide comparable results to the large-area reference module approach.

The G_E derived from I_{SC} measurements of a 24-module string agreed to module-level G_E measurements within 2.5% or better when G_E was near one-sun. Although the string-level I-V measurements were limited to three clear days, the results are encouraging that continuous string-level I-V scans (e.g., made by inverters) can be used to estimate G_E of healthy bifacial PV arrays. We leave deeper investigations of effective irradiance modeling via string-level I-V for future work.

We examined spectral effects in R_{POA} measurements. Although the spectral distribution of R_{POA} differed significantly from the AM1.5G reference, the overall impact of rear spectral mismatch is less than 1% when considering that the dominant contribution to bifacial performance is frontside irradiance.

We also evaluated the potential of bifacial reference panels to measure cell temperature with V_{OC} measurements. We found mean absolute errors of 2.5°C and 2.1°C when performing this method with module and string-level bifacial measurements, respectively. This level of error translates to approximately 1% uncertainty in power measurements of modern Silicon modules. Thus, the V_{OC} data can add value to continuous I-V measurements by offering a method that avoids the rear-side shading created by conventional module temperature sensors.

It was shown that bifacial performance ratios can vary by 3% based on the placement and type of small-area sensor used for R_{POA} measurements. Using bifacial reference panels for performance ratio calculations can reduce this variation because they circumvent the need to identify representative small-area sensor locations.

Finally, we used the G_E data to predict string-level power. G_E data from pyranometers, reference cells and reference modules resulted in 2.9–3.4% average errors relative to measured power. The comparable prediction errors between traceable small-area irradiance sensors and calibrated modules suggests that reference modules are a suitable and accurate approach for measuring irradiance in bifacial systems.

V. Conclusion

This work investigated the capability of bifacial modules, calibrated per the single-side equivalent irradiance method of IEC TS 60904-1-2, to be used as large-area sensors that measure R_{POA} and G_E. A supplemental monofacial reference module was used in the field to decouple the rear irradiance R_{POA} from the effective irradiance G_E. We compared the reference module measurements to three types of commonly used small-area sensors, all with traceable calibrations.

Out of all the small-area sensors tested, we found that reference cell measurements of R_{POA} and G_E had the best agreement to those made by reference modules. The array of 3–4 rear facing sensors showed that a single small-area R_{POA} sensor location can agree to large-area reference module R_{POA} measurements by 4 W/m^2 absolute, 9% relative. PVWatts yield predictions that used G_E data from pyranometers, reference cells, and modules were within 2.9%–3.4% of measured string-level power, thereby demonstrating the absolute accuracy of the bifacial reference module approach.

We found that the choice of small-area sensor type and mounting location adds at least ±1.5% uncertainty to bifacial performance ratio calculations. Calibrated reference modules can be used to reduce said variation in bifacial performance ratio calculations, while at the same time simplifying the monitoring system design and offering the ability to estimate cell temperature through the V_{OC} of the I-V curve.

Acknowledgements

VI. References

[1] J. Stein et al., "Bifacial Photovoltaic Modules and Systems: Experience and Results from International Research and Pilot Applications," IEA PVPS Task 13, 2021.

[2] IEC TS 60904-1-2 "Measurement of current-voltage characteristics of bifacial photovoltaic (PV) devices", 2019.

[3] IEC 61724-1 Edition 2 "Photovoltaic system performance - Part 1: Monitoring", 2021.

[4] M. Waters et al., "Suggested Modifications for Bifacial Capacity Testing," in *46th IEEE PVSC*, Chicago, IL, 2019.

[5] A. Gracia-Amillo et al., "Extension of energy rating to bifacial modules – proposals from the PV-enerate project," JRC Technical Report, 2020.

[6] M. Gostein et al., "Measuring Irradiance for Bifacial PV Systems," in *IEEE 48th PVSC*, 2021.

[7] S. A. Pelaez et al., "Model and Validation of Single-Axis Tracking with Bifacial PV," *IEEE JPV,* vol. 9, no. 3, pp. 715-721, 2019.

[8] C. Deline et al., "Estimating and parameterizing mismatch power loss in bifacial photovoltaic systems," *PiP,* vol. 28, no. 7, 2020.

[9] G. Janssen et al., "Impact of inhomogenous irradiance at the rear of bifacial panels on modelled energy yield," in *33rd EUPVSEC*, 2017.

[10] S. Pelaez et al., "Effect of torque-tube parameters on rear-irradiance for bifacial PV on trackers," in *46th IEEE PVSC*, Chicago, 2019.

[11] C. Zhao et al., "Accurate shading factor and mismatch loss analysis of bifacial HSAT systems through ray-tracing modeling," *Solar Energy Advances,* vol. 1, 2021.

[12] J. C. Blakesley et al., "Effective spectral albedo from satellite data for bifacial gain calculations of PV systems," in *36th EUPVSEC*, 2020.

[13] M. Gostein, B. Marion and B. Stueve, "Spectral Effects in Albedo and Rearside Irradiance Measurement for Bifacial Performance," in *47th IEEE PVSC*, 2020.

[14] N. Riedel-Lyngskær et al., "The effect of spectral albedo in bifacial performance," *Sol. Energy,* vol. 231, no. 1, pp. 921-935, 2022.

[15] A. Asgharzadeh et al., "A Benchmark and Validation of Bifacial PV Irradiance Models," *46th IEEE PVSC,* 2019.

[16] S. Peleaz et al., "Field-Array Benchmark of Commercial Bifacial PV Technologies with Publicly Available Data," in *47th IEEE PVSC*, Calgary, 2020.

[17] P. Babal et al., "Uncertainties in irradiance measurements of sensors to POA-rear of bifacial solar panels," in *47th IEEE PVSC*, Calgary, 2020 .

[18] N. Riedel-Lyngskær et al., "Validation of Bifacial Photovoltaic Simulation Software against Monitoring Data from Systems in Denmark," *Applied Sciences,* vol. 10, no. 23, pp. 1-29, 2020.

[19] J. Polo, W. Fernandez-Neira and M. Alonso-Garcia, "On the use of reference modules as irradiance sensor for monitoring and modelling rooftop PV systems," *Renewable Energy,* vol. 106, pp. 186-191, 2017.

[20] Y. Hishikawa et al., "Improved precision of the outdoor performance measurements of photovoltaic modules by using the photovoltaic irradiance sensor," *Sol. Energy,* vol. 211, pp. 85-89, 2020.

[21] J. Braid et al., "Effective Irradiance Monitoring Using Reference Modules," in *49th IEEE PVSC*, Philadelphia, 2022.

[22] N. Riedel-Lyngskær et al., "Value of bifacial photovoltaics used with highly reflective ground materials on single- axis trackers and fixed-tilt systems: a Danish case study," *IET RPG,* vol. 14, pp. 3946-3953, 2021.

[23] S. Chunduri and M. Schmela, "Very High-Power Solar Modules," TaiyangNews, 2021.

[24] VDMA, "International Technology Roadmap for Photovoltaics (ITRPV): 2021 Results," 2022.

[25] S. Spataru et al., "Monitoring and Fault Detection in PV Systems Based On Inverter Measured I-V Curves," in *31st EUPVSEC*, Hamburg, 2015.

[26] C. Deline and S. Pelaez, "bifacial_radiance: a python package for modeling bifacial solar photovoltaic systems.," *Journal of Open Source Software,* vol. 5, no. 50, 17 Dec 2020.

[27] S. Pelaez, C. Deline, J. Alderman, M. Mikofski and C. Stark, "bifacial_radiance: a python package for modeling bifacial solar photovoltaic systems," 27 May 2020. [Online].

[28] M. Anoma et al., "View Factor Model and Validation for Bifacial PV on Single-Axis Trackers," in *44th IEEE PVSC*, Washington D.C., 2017.

[29] D. Dirnberger and U. Kräling, "Uncertainty in PV Module Measurement—Part I: Calibration of Crystalline and Thin-Film Modules," *IEEE JPV,* vol. 3, no. 3, pp. 1016-1026, 2013.

[30] G. Koutsourakis et al., "Results of the Bifacial PV Cells and PV Modules Power Measurement Round Robin Activity of the PV-Enerate Project," in *37th EUPVSEC*, 2021.

[31] M. Korevaar et al., "Novel Soiling Detection System for Solar Panels," in *33rd EUPVSEC*, Amsterdam, 2017.

[32] M. Korevaar et al., "Simulation and Validation of Bifacial Irradiance Sensor Mounting Position," in *37th EUPVSEC*, Lisbon, 2020.

[33] IEC 60904-7 Ed. 4.0, 2019.

[34] IEC 60904-3 Ed. 4.0, 2019.

[35] A. Driesse and W. Zaaiman, "Characterization of Global Irradiance Sensors for use with PV Systems," in *42nd IEEE PVSC*, 2015.

[36] L. Dunn, M. Gostein and K. Emery, "Comparison of Pyranometers vs. PV Reference Cells for Evaluation of PV Array Performance," in *39th IEEE PVSC*, 2012.

[37] D. Myers and C. Gueymard, "Description and availability of the SMARTS spectral model for photovoltaic applications," in *Proceedings of SPIE - The International Society for Optical Engineering*, 2004.

[38] IEC 60904-5 Ed. 2.0, 2011.

[39] S. Zhang et al., "Illumination-dependent temperature coefficients of the electrical parameters of modern silicon solar cell architectures," *Nano Energy,* vol. 98, 2022.

[40] D. King, B. Boyson and J. Kratochvill, "Photovoltaic Array Performance Model," Sandia Report (SAND2004-3535), 2004.

[41] M. Chowdhury et al., "Sensitivity analysis of the state of the art PV temperature estimation methods," in *IEEE 48th PVSC*, Miami, 2021.

[42] S. Krauter and A. Preiss, "Comparison of module temperature measurement methods," in *34th IEEE PVSC*, Philadelphia, 2009.

[43] R. Smith, "Improving Long-Term Back-of-Module Temperature Measurements," SolarPro Magazine, May/June 2015.

[44] N. Reich et al., "Performance ratio revisited: is PR > 90% realistic?," *PiP,* vol. 20, pp. 717-726, 2012.

[45] A. Dobos, "PVWatts Version 5 Manual," National Renewable Energy Laboratory, 2014.